Earth and Planetary Science Letters

Dolostone dry pulverization and cementation induced by coseismic rapid decompression of CO2-rich gas: first natural example from an active seismic and hydrothermal extensional domain (Matese, Apennines, Italy)

--Manuscript Draft--

Manuscript Number:	
Article Type:	Letters
Keywords:	pulverized rock, CO2, earthquake, gas, dolostone
Corresponding Author:	Andrea Billi, PhD Consiglio Nazionale delle Ricerche Rome, ITALY
First Author:	Andrea Billi, PhD
Order of Authors:	Andrea Billi, PhD
	Luca Smeraglia
	Luca Aldega
	Fabrizio Balsamo
	Marino Domenico Barberio
	Chiara Boschi
	Antonio Caracausi
	Eugenio Carminati
	Alessandro Iannace
	Marco Mercuri
	Mattia Pizzati
	Stefano Tavani
Abstract:	South Matese is a hydrothermally and seismically active extensional area characterized by intense CO 2 outgassing and Mw ≤7.1 earthquakes. There, meters-sized pockets of incoherent pulverized dolostone are hosted within the Mesozoic carbonate succession at the hanging wall of regional normal faults. The aim of this paper is to understand the pulverization process. The pulverized dolostone is finely comminuted (5–200 μm), but primary structures, such as bedding, are preserved. The grain size distribution is similar to that of previously studied pulverized rocks associated with active faults and dissimilar to that of carbonate cataclasites and fault gouges. The pulverized pockets are surrounded by a sort of halo in which the loose grains are cemented, in their original position, by microsparry calcite, thus resulting in a cemented micro-mosaic breccia. Stable isotopes from the cement are compatible with calcite precipitation from rapidly degassing shallow waters. Supported by previous laboratory experiments, the pulverized dolostone is interpreted as resulting from local accumulations of pressurized CO 2 -rich gas, suddenly decompressed likely during earthquakes. The limited permeability of the gas-saturated dolostone prevented a prompt escape of the gas from the rock, which was therefore pulverized by the rapid expansion of the trapped gas. The sudden decompression as well as the porosity increase enhanced by the rock pulverization attracted bicarbonate-rich groundwaters, from which microsparry calcite cement rapidly precipitated, fossilizing the newly pulverized dolostone. The precipitation formed an impermeable barrier around the pulverized pockets, which, therefore, remained internally incoherent and dry. This process should have occurred above the CO 2 subcritical–supercritical boundary at depths of ~800 m. The proposed mechanism is hypothesized for the first time in an active tectonic environment and may improve our knowledge of possible chemical-physical processes connected with the subsurface storage of CO 2 in seismically active areas.

Suggested Reviewers:	Thomas Mitchell tom.mitchell@ucl.ac.uk expert of pulverizd rocks
	Marieke Rempe marieke.rempe@rub.de expert of pulverized rocks
	Steven Smith steven.smith@otago.ac.nz expert of pulverized crocks
	Michele Fondriest michelefondriest@yahoo.it
	Thomas Rockwell trockwell@sdsu.edu expert of pulverized rocks
Opposed Reviewers:	

Dear Editor of EPSL,

please find enclosed the manuscript titled “Dolostone dry pulverization and cementation induced by coseismic rapid decompression of CO2-rich gas: first natural example from an active seismic and hydrothermal extensional domain (Matese, Apennines, Italy)” by Billi et alii.

I would be very grateful if you could consider this manuscript for its publication on EPSL after proper reviews.

Looking forward to hearing from you

Sincerely

Andrea Billi

Dolostone dry pulverization and cementation induced by coseismic rapid decompression of CO_2-rich gas: first natural example from an active seismic and hydrothermal extensional domain (Matese, Apennines, Italy)

Andrea Billi[1*], Luca Smeraglia[1], Luca Aldega[2], Fabrizio Balsamo[3], Marino Domenico Barberio[2], Chiara Boschi[4], Antonio Caracausi[5], Eugenio Carminati[2], Alessandro Iannace[6], Marco Mercuri[2], Mattia Pizzati[3], Stefano Tavani[1,6]

[1] Consiglio Nazionale delle Ricerche, IGAG, Rome, Italy.

[2] Department of Earth Sciences, Sapienza University of Rome, Italy.

[3] Department of Chemistry, Life Sciences and Environmental Sustainability, University of Parma, Italy.

[4] Consiglio Nazionale delle Ricerche, IGG, Pisa, Italy.

[5] Istituto Nazionale di Geofisica e Vulcanologia, Palermo, Italy.

[6] Dipartimento di Scienze della Terra, dell'Ambiente e delle Risorse, University of Naples, Italy.

[*] corresponding author: Andrea Billi, Consiglio Nazionale delle Ricerche, IGAG, at Department of Earth Sciences, Sapienza University of Rome, Geochimica Building, P.le A. Moro 5, 00185, Rome, andrea.billi@cnr.it

Abstract

South Matese is a hydrothermally and seismically active extensional area characterized by intense CO_2 outgassing and Mw ≤7.1 earthquakes. There, meters-sized pockets of incoherent pulverized dolostone are hosted within the Mesozoic carbonate succession at the hanging wall of regional normal faults. The aim of this paper is to understand the pulverization process. The pulverized dolostone is finely comminuted (5–200 μm), but primary structures, such as bedding, are preserved. The grain size distribution is similar to that of previously studied pulverized rocks associated with active faults and dissimilar to that of carbonate cataclasites and fault gouges. The pulverized pockets are surrounded by a sort of halo in which the loose grains are cemented, in their original position, by microsparry calcite, thus resulting in a cemented micro-mosaic breccia. Stable isotopes from the cement are compatible with calcite precipitation from rapidly degassing shallow waters. Supported by previous laboratory experiments, the pulverized dolostone is interpreted as resulting from local accumulations of pressurized CO_2-rich gas, suddenly decompressed likely during earthquakes. The limited permeability of the gas-saturated dolostone prevented a prompt escape of the gas from the rock, which was therefore pulverized by the rapid expansion of the trapped gas. The sudden decompression as well as the porosity increase enhanced by the rock pulverization attracted bicarbonate-rich groundwaters, from which microsparry calcite cement rapidly precipitated, fossilizing the newly pulverized dolostone. The precipitation formed an impermeable barrier around the pulverized pockets, which, therefore, remained internally incoherent and dry. This process should have occurred above the CO_2 subcritical–supercritical boundary at depths of ~800 m. The proposed mechanism is hypothesized for the first time in an active tectonic environment and may improve our knowledge of possible chemical-physical processes connected with the subsurface storage of CO_2 in seismically active areas.

1. Introduction

Pulverized rocks are extremely comminuted low-strain rocks in which the micro-clasts are still almost in their original position such as to resemble a micro jigsaw puzzle. Pulverized rocks are typically found in low permeability rocks, such as crystalline or tight carbonate rocks, and even when these rocks occur within fault zones (as it usually happens), they are markedly different from cataclastic rocks and fault gouges for grain size distribution, texture, and position within the deformation zone (Brune, 2001; Dor et al., 2006; Rockwell et al., 2009; Muto et al., 2015; Schröckenfuchs et al., 2015; Williams et al., 2021).

Because of these peculiar structural features and their occurrence within seismically active fault zones, pulverized rocks are often considered as diagnostic of high-strain-rate deformation (e.g., earthquakes) within shallow (<3 km depth) confined volumes of rock (Wilson et al., 2005; Doan and Gary, 2009; Mitchell et al., 2011; Sagy and Korngreen, 2012; Aben et al., 2017; Fondriest et al., 2017; Rodríguez-Escudero et al., 2020; Ostermeijer et al., 2022). In other words, when a sudden oversupply of energy (e.g., coseismic energy) enters a rock volume, it cannot always be localized and accommodated along a single fracture (e.g., a fault surface), and thus the rock can be suddenly comminuted by a myriad of pervading dilational micro-fractures (Rempe et al., 2013). This mechanism is thought to be possible, but hardly observed at large confining pressures (i.e., at great depths) that would greatly suppress the ability of rock to expand (Yuan et al., 2011).

One interesting but poorly investigated (in active tectonic environments) mechanism of pulverization is the mechanism connected with fluid (gas) pressure fluctuation within rocks. To this end, Mitchell et al. (2013) experimented with explosive pulverization of rocks in a laboratory by imparting rapid drops in gas confining pressure for noble gas-saturated rock samples (tonalite), using a specifically designed pressure vessel to allow near-

instantaneous decompression of the rock samples. The limited permeability of the tested rocks created non-draining conditions during the rapid decompression experiments, resulting in the pulverization of the tonalite due to the sudden expansion of the gas trapped within the rock pores, unable to drain quickly from the rock (Mitchell et al., 2013). These promising laboratory experiments were not supported by validation on natural examples; hence, the pulverization mechanism via rapid decompression of gases within rocks remains experimentally operable but still elusive in nature, at least in active fault zones. It is noteworthy, in fact, that similar processes of rock disruption through rapid decompression of gases have been experimentally well-tested and applied to other Earth's sciences, such as volcanology (e.g., Alidibirov and Dingwell, 1996) and coal mining (e.g., Wang et al., 2015; Pan et al., 2020).

In this work, we present a multidisciplinary analysis of pulverized dolostone exposed in the hanging wall of the south Matese normal fault system, southern Apennines, Italy (Fig. 1a). This site is ideal to study possible relationships between natural faulting, active fluid circulation, and rock pulverization in a seismically active region. The study area is indeed characterized by (1) seismically active normal faults (Boncio et al., 2022), (2) extensive exposure of dolostone, which is a rock type elsewhere documented to be often pulverized (Agosta and Aydin, 2006; Sagy and Korngreen, 2012; Schröckenfuchs et al., 2015; Fondriest et al., 2017; Kaminskaite et al., 2020), and (3) active circulation of CO_2-rich fluids (Figs. 1b and 1c) that may partially derive from the nearby active or quiescent volcanic districts (Di Luccio et al., 2018; Santo et al., 2019). Our main goal is to understand the mechanism of dolostone pulverization. Our results are compatible with dolostone dry pulverization and subsequent calcite precipitation driven by the (coseismic) rapid decompression of CO_2-rich gases. Moreover, we believe that this research may improve our knowledge regarding possible chemical and physical processes connected with the subsurface storage of CO_2.

2. Geological Setting

The studied exposure (Figs. 1–3) is located in the central-southern Apennines, a Late Oligocene to Present fold-thrust belt generated by the eastward retreat of the west-dipping subduction of the Adriatic plate below the European continental margin (Malinverno and Ryan, 1986). Orogenic accretion was mainly accommodated through a set of NE-verging thrust systems, which scraped off the pre- and syn-orogenic deposits of the Adriatic plate. In the study area, the pre-orogenic deposits consist of 4,000–5,000 m-thick Late Triassic–Cretaceous shallow-water limestones and dolostones. These carbonates are unconformably covered by nearly 3 km of syn-orogenic foredeep-filling sediments, which include middle Miocene shallow-water carbonates, Tortonian hemipelagic marls, and Late Miocene siliciclastic turbidites. Thrust faults developed during wedge accretion and juxtaposed pre-orogenic deposits onto syn-orogenic sediments, generating stacks of multiple thrust sheets from the surface down to ~10 km depth (Mostardini and Merlini, 1986).

Since the Early Pliocene, the internal (west) and axial part of the central-southern Apennines belt underwent post-orogenic exhumation and extensional faulting associated with the development of the Tyrrhenian back-arc basin (Malinverno and Ryan, 1986). This extensional regime is still active and has generated a peri-Tyrrhenian volcanic system and a set of main NW-SE oriented extensional faults that are the source of Mw ≤7.1 historical and instrumental seismicity (Boncio et al., 2022) as well as the path of active degassing (Ascione et al., 2018). We focused our study on the Ailano area, which is located at the southern foot of the Matese Mts., on the hanging wall of the south Matese active normal fault system, nearby active or quiescent volcanic-hydrothermal districts (Fig. 1).

In the Ailano area, the exposed stratigraphic sequence is characterized by Upper Triassic carbonate platform dolostone, upward followed by Lower Jurassic to Upper

Cretaceous carbonate platform limestone and dolostone, and by syn-orogenic siliciclastic deposits (Fig. 1a). Some emersion-related clay-rich layers interbedded within the carbonates are known to exist in the early Mesozoic portion of the sequence. Based on the minimum thickness of the sedimentary pile overlying the study outcrop, we infer that the investigated area has been exhumed from a minimum depth of about 3.5 km. Obviously, as will be discussed below, the exhumation depth does not necessarily represent the depth of dolostone pulverization discussed in this paper.

In the study area, the stratigraphic succession is cut by a network of NW-SE, NE-SW, and E-W oriented extensional faults, which generated carbonate ridges and valleys filled by travertine, lacustrine, and alluvial deposits. The main fault system is, however, the NW-striking NW-dipping normal fault occurring to the NE of the investigated area, at the foot of the Matese Mts. The investigated area is therefore located on a wide and fractured-faulted hanging wall block (Fig. 1a). The subsurface structural architecture of this hanging wall block is substantially unknown. Due to the presence of numerous active normal faults and associated degassing vents in the study area, we hypothesize, however, the presence of a set of fluid-conductive normal fault zones beneath the studied exposure (see the cross-section in Fig. 1a). This hypothesis is corroborated by the outcrop-scale faults and fractures observed in the exposure (Fig. 2a).

The studied exposure is located ~1 km to the SW of the village of Pratella, within the NE-dipping strata of Lower Jurassic carbonate platform limestone and dolostone (Figs. 1a). As mentioned above, the exposure is located on the broad hanging wall of the NW-SE trending south Matese normal fault system, including the ~20 km-long Aquae Iuliae Fault, which likely generated the 1349 Mw 6.7 earthquake, one of the most catastrophic events experienced along the Apennines. The seismically active south Matese normal fault system generated additional strong (Mw ≤7.1) historical earthquakes (Boncio et al., 2022).

3. Hydrothermal Setting

Large amounts of deeply sourced volatiles (e.g., CO_2, helium) are released from volcanoes (active volcanoes: Vesuvius, Phlegrean Fields; quiescent volcanoes: Roccamonfina, Vulture) and adjacent tectonically active regions in central-southern Italy, including the study area. At depth, the gas accumulates in crustal traps, generating CO_2-pressurized reservoirs that can trigger seismicity (Di Luccio et al., 2018). Often, in correspondence to these deep natural CO_2 reservoirs, several CO_2-venting seeps occur at the surface (e.g., Chiodini et al., 2010). In the study area, CO_2- and CH_4-rich (up to 30.000 g x d^{-1} and 2000 g x d^{-1} respectively; Ascione et al., 2018) gas vents and large diffusive gas emissions from soils occur close to the villages of Ciorlano and Ailano (Fig. 1). Geochemical investigations recognized that mantle-derived fluids (e.g., CO_2, helium) are involved in the local seismicity (e.g., Caracausi and Paternoster, 2015; Di Luccio et al., 2018). Furthermore, the groundwater circulating through the carbonate aquifers contains large amounts of deep CO_2. The total amount of deeply derived CO_2 transported in solution by the groundwater for the entire Matese aquifer is ~570 metric tons day^{-1} (Di Luccio et al., 2018). Combining the deep carbon from natural gas emissions (vents and diffusive degassing from soils) and dissolved in groundwater, this area emits amounts of deep carbon even larger than those emitted from some active volcanic systems (e.g., Ascione et al., 2018; Di Luccio et al. 2018). The volatiles in the Matese area mainly degas from active fault zones, suggesting a control by active tectonics over fluid circulation (Ascione et al., 2018).

The helium in the fluids emitted from the Matese area has a mantle component. Its isotopic signature is between 0.7 and 1 Ra (Fig. 1c, Table S1; Caracausi and Paternoster, 2015; Ascione et al., 2018; unpublished INGV data), larger than typical crustal fluid values (0.01–0.03 Ra) from cratons and sedimentary basins far from active tectonic regions (Fig.

1c). In contrast, the C/^{4}He ratios in the same fluids fall within 1.9 x 10^4 and 1.6 x 10^5. The diagram of C/^{4}He vs. R/Ra (Fig. 1c) clearly indicates that He in the Ailano-Ciorlano gases results from a mixing of mantle and crust components. Considering that these gas emissions occur in a restricted area (<10 km^2), it is, however, unlikely that: (1) different C sources/production contributed to the different sites and at different times, and (2) there is a different production of ^{4}He from U and Th within the rocks. Hence, different (or variable) C/(U+Th) are not the reason for the C/^{4}He variability in the Ailano-Ciorlano fluids. Alternative reasons may include fractionation processes and/or gas–water interaction that can easily modify the C/He ratio of gases that are trapped in natural reservoirs or during their transfer towards the atmosphere (O'Nions and Oxburgh, 1988). For instance, a partial dissolution of CO_2 and He in water (gas–water interaction at depth) can be the origin of a decreasing C/^{4}He ratio (e.g., Randazzo et al., 2021) due to their different solubility in water (CO_2 >He). In addition, previous studies (Italiano et al., 2000; Di Luccio et al., 2018), combining geochemical and geophysical analyses with an excess of heat flow, inferred that the presence of magmatic melts at depth beneath the Matese region and the ascent of fluids along lithospheric faults perturb the thermal state at the regional scale and support the high flux of volatiles at the surface.

4. Methods

We collected data and rock samples (Table S2) along a NE-SW trending ~200 m long road cut, where fractured Lower Jurassic platform carbonates and discrete zones of pulverized carbonates are exposed (Figs. 2 and 3; Lat. 41.397729°, Long. 14.171114°). To understand the origin of the pulverized carbonates, we combined the following analytical techniques on both the pulverized rocks and the surrounding host rock: (1) outcrop-scale geological and structural observations and analyses; (2) thin section analysis under optical

199 microscope and associated cathodoluminescence, and under electronic microscope (SEM)
200 and associated Energy Dispersive Spectrometry (EDS); (3) grain size distribution analyses
201 (2D image analysis and 3D laser diffraction granulometry on cohesive and incohesive
202 samples, respectively); (4) X-ray diffraction analyses; (5) geochemical analyses of major
203 and minor elements and rare earth elements (REE); and (6) carbon and oxygen stable
204 isotope analyses. All methods are described in detail in the Supplemental Material.

205

206 ## *5. Results*

207 ### *5.1 Field Observations*

208 Along the studied exposure, we recognized two main types of rocks relevant to our
209 research (Figs. 2 and 3): (1) host carbonates (mainly dolostone) displaying bedding and (2)
210 pockets of incohesive pulverized carbonates (mainly dolostone) hosted within the bedded
211 carbonates. As we will detail below, in some cases, we differentiate distal and proximal host
212 rocks based on the distance from the pulverized pockets (distal: >10 m; proximal: <20 cm).
213 An angular unconformity marked by overlying Quaternary breccias truncates the upper part
214 of the exposure, made of pulverized dolostone and bedded carbonates (Fig. 2b).

215 The host rock consists of decimeters-thick beds of dolostone and dolomitic limestone
216 as well as rarer limestone that are fractured and faulted (Fig. 2a). The beds are NE-dipping
217 by about 45°. Fractures are very frequent (fracture spacing is often about 1 cm or less) and
218 hardly systematic, although main sets include fractures striking NW–SE and dipping toward
219 either NE or SW by about 70° or more. Faults are less frequent than joints (only 17) and with
220 very limited displacements (less than a few centimeters). Fault surfaces strike preferentially
221 NW–SE, with a dip angle of about 60°, either toward NE or toward SW. A set of faults, N–S
222 striking and dipping toward E by about 70°, is also present (Fig. 2a; Table S3). It is significant

223 that, while appearing compact and cohesive, when the host rock in the vicinity (<10–15 cm)
224 of the pulverized pockets is fractured with the hammer, inside it often shows small (<1 cm
225 in size) pockets or tubercles of incohesive pulverized material.

226 The pulverized pockets are meters-sized and characterized by irregular or
227 chimney/domal morphologies. Pulverized dolostone is usually white in color, totally
228 incohesive, very fine-grained, and shows jagged or transitional to sharp boundaries with the
229 fractured host rock (Figs. 2 and 3; Videos S1-S4; Virtual Outcrops S1-S4). Within the
230 pulverized pockets, primary bedding is in many cases still visible (Figs. 2b, 2c, and 3a; Video
231 S4). Pebble-sized fragments of the host rock are occasionally found within the fine-grained
232 matrix of the pulverized dolostone (Fig. 3b). The domal pockets of pulverized dolostone
233 appear, in some cases, upwardly bounded by a thin (2–5 cm) layer of shale or clayey marl
234 occurring along the bedded host dolostone. At least in one case, the shale layer has an
235 antiformal geometry around the upper portion of a domal pocket of pulverized rocks (Fig.
236 3e).

237

238 ***5.2 Microscopic Observations***

239 The host rocks collected near (proximal) and far away (distal) from the studied
240 pulverized pockets are characterized by a large variety of depositional/diagenetic
241 microstructures, which are well preserved in some cases (Fig. 4). In the distal host rock,
242 primary features are calcareous grainstones, where peloids, lumps, and some algae are
243 perfectly preserved together with intergranular early phreatic cements and late diagenetic
244 blocky calcite (Fig. 4a). Fine-grained crystalline dolomites display an excellent preservation
245 of the grainstone depositional texture (Fig. 4b). In places, incomplete replacement of
246 limestone by dolomite is recorded (Fig. 4b). A zoned and coarse crystalline dolomite within
247 fractures and cavities and poikilotopic calcite occur (Fig. 4c), probably representing

hydrothermal dolomitization. These microfacies are typical of Mesozoic shallow water carbonates from the central Apennine carbonate platform.

SEM observations, together with EDS analyses, revealed that the dolomite (of both distal and proximal host rocks) consists of fine-grained crystals (Figs. 5a–5c, S1, and S2). In places, dolomite crystal boundaries are visible (Figs. 5a, 5b, and S1), while in other cases, the crystals are well welded (Figs. 5c and S1). Intergranular porosity occurs between the crystals (Figs. 5a–5c, S1e-S1h, and S3a). Occasionally, calcite-filled veins crosscut the fine-grained dolomite crystals (Figs. 5a and S2c–S2e).

Under optical microscope, the proximal host rock surrounding and embedding the pulverized carbonates is characterized by banded zones alternating with different colors and locally concentric geometry (Figs. 4d and 4e). Sedimentary structures are preserved or still decipherable within the banded zones (Figs. 4c and 4d), which consist of fine-grained dolostone crystals showing equal grain sizes (Figs. 4e and 4f). The fine-grained dolostone crystals are non-luminescent (Figs. 4g, 4h, and S4a–S4f) and, in places, are cut by <1 mm thick microfractures filled by blocky calcite crystals showing a dull red and zoned luminescence color (Figs. 4g and 4h).

SEM observations reveal the micro-texture of the proximal host rock, which consists of grains immersed in a microsparry calcite and each one formed by single crystals or more often by aggregates of dolomite crystals. The resulting pattern is a cemented micro mosaic or crackle-like breccia (Fig. 5e-5i, S2c-S2g, S3b, and S3c). The microsparry (microcrystalline) calcite cement displays a dominant black color under cathodoluminescence, with rare bright orange rims along the outer crystal edges (Fig. S4e and S4f). No substantial shear displacement is observed along the microfractures (i.e. between the grains), which are non-systematically oriented and mostly coincide with the crystal (or crystal–aggregate) boundaries. The dolomite crystals contain widespread

micropores (Figs. 5e, 5f, S1f–S1h, S3a, and S3b). Crystal boundaries are generally sharp; however, in places, these boundaries may be rounded, showing embayment-like morphologies (Figs. 5e, 5f, S2c, and S2d). The transition toward bands dominated by microcrystalline calcite cement is diffuse and is characterized by dolomite crystals fading within the calcite cement (Figs. 5f and S2d). Small, rounded pockets of fine (pulverized) dolomite grains also occur (Figs. 5h, 5i, and S2e-S2g). In these pockets, no calcite cement is present while, in contrast, calcite cement is present all around them. Occasionally, <100 µm thick calcite filled veins cut across the dolomite crystals (Figs. 5g, 5i, and S2g).

At the micro-scale, pulverized incohesive carbonates (sampled within the pulverized pockets) consist of dolostone grains with sharp boundaries (Figs. 5k, 5l, S2h, and S3d). In places, the rhombohedral habit of dolostone crystals is still preserved, although the crystal faces are often characterized by small cavities (Figs. 5k-l, S2h, and S3d). The dolostone grains consist of single crystals or, more often, crystal aggregates.

5.3 Grain Size Distributions

Distal host rocks (dolostone; e.g., Figs. 5a-5c) show mean grain diameters (computed from 2D analyses) between 10.5 and 47.8 µm, with characteristic unimodal distribution (Fig. 6a). In these rocks, grains span between 10 and 100 µm and clearly coincide with the size of dolomite crystals. Proximal host rocks (cemented mosaic breccias; e.g. Figs. 5d–5f) also show unimodal distribution (computed from 2D analyses), with a mean grain diameter spanning from 66.3 to 86.1 µm (Fig. 6b), coinciding with the size of single dolomite crystals or aggregates of a few crystals. The grain size in loose pulverized rocks (dolostone grains from pulverized pockest; Figs. 5k and 5l) span between 5 and 200 µm (computed from 3D analyses) and show mean grain diameters in the range 57.8 to 153 µm, also with unimodal distribution (Fig. 6c). SEM observations on the loose pulverized dolostone show that the

298 grains are made up of individual dolomite crystals of 20–30 μm in size or by dolomite crystal
299 aggregates of 70–90 μm (Figs. 5k, 5l, S2h and S3d). All results from grain size analyses are
300 summarized in Tables S4 and S5 and in Figs. S5–S18.

301

302 ***5.4 Bulk X-Ray Diffraction***

303 We performed X-ray semiquantitative analyses of the bulk composition of eleven
304 samples from the host rock (proximal and distal), ten samples from the pulverized dolostone,
305 and three samples from the shale or clayey marl occurring along the bedded host rock (Fig.
306 7 and Table S6). The distal host carbonates include two endmembers: the first one is
307 characterized by high dolomite amounts between 91 and 93% and low calcite contents (7–
308 9%), and the second one is entirely composed of calcite (99%) and has a very low dolomite
309 content, not exceeding 1% (Fig. 7). The remaining samples from the host rock (proximal)
310 show variable amounts of dolomite, in the range of 63 to 98% (average 81%), and calcite,
311 between 2 and 37% (average 19%; Fig. 7). The pulverized rocks show greater amounts of
312 dolomite (from 85 to 100%, average 98%) and smaller amounts of calcite (from 0 to 10%,
313 average 2%; Fig. 7) than their counterparts in the host rock. Occasionally, sheet silicates
314 occur in the pulverized rocks, with contents lower than 6% (Fig. 7). In a few pulverized
315 samples, traces of norsethite $BaMg(CO_3)_2$, a mineral belonging to the dolomite group, occur.
316 Shale interbedded with dolostone layers contain sheet silicates (mica, chlorite, and kaolinite)
317 with amounts ranging between 70 and 89%, calcite (6–24%), hematite (2–4%), and minor
318 amounts of quartz (1–2%) and dolomite (1–2%) (Fig. 7). In places, traces of gypsum were
319 observed in the X-ray tracings (Supplemental Diffractograms).

320

321 ***5.5 Bulk and Punctual Analyses of Stable Isotopes***

Stable isotope analyses show that both (proximal and distal) host rocks and pulverized dolostone are characterized by similar values of $\delta^{13}C$ and $\delta^{18}O$ (Fig. 8a and Table S7). We acknowledge that these results refer to bulk analysis (i.e., without separating dolomite and calcite components in the samples). In particular, $\delta^{13}C$ values show a narrow range, between +2.5 ‰ and +4.0 ‰ V-PDB, whereas $\delta^{18}O$ values range between +28.0 ‰ and +33.0 ‰ V-SMOW (Fig. 8a). Such values are typical for most marine carbonates, particularly the Jurassic-Cretaceous ones in the central Apennines (e.g., Agosta and Kirschner, 2003).

We also performed punctual stable isotope analyses on eight micro subsamples that were collected along a centimeter-scale transect across banded calcite in a proximal host rock (see the A1.1 sample in Fig. S19). Similar banded calcite is visible nearby cemented mosaic breccias also in Figs. 5d, 5f, and S2d. The $\delta^{18}O$ values show a narrow range, between +26.0 ‰ and +28.0 ‰, whereas the $\delta^{13}C$ values show a wide range, between +3.0 ‰ and +8.0 ‰ (see the A1.1 sample in Figs. 8a and 8b).

5.6 Bulk Analysis of REE and Minor Chemical Elements

Bulk analyses (i.e., without separating dolomite and calcite components in the samples) of REE (rare Earth elements) and minor chemical elements from (distal and proximal) host rocks and pulverized dolostone show similar patterns (Figs. 8c and 8d, Table S8). In particular, minor element concentration spans from 0.01 ppm to 1,000 ppm. The abundance of REE in pulverized dolostone and host rocks show large variations, ranging from 0.0020 ppm to 0.025 ppm. No anomalous concentrations were observed (Figs. 8c and 8d).

The PAAS-normalized (Post-Archean Australian Shales) patterns show that the REE concentrations in the host rock and in the pulverized dolostone are in the range that is typical for the Mesozoic carbonates in the central Apennines (Fig. 8d; Castorina et al. 2020). Most samples show a negative Ce anomaly (Fig. 8d), typical of marine carbonates, and La/Sm and La/Yb ratios <1 (Fig. 8d), typical of carbonate rocks in late diagenetic conditions (Fig. 8d).

6. Discussion

6.1 Pulverized Rocks

Before dealing with the pulverization process, the first issue to be discussed is whether the studied rocks are truly pulverized rocks (sensu Brune, 2001 and Dor et al., 2006). The following features suggest a pulverized nature of the studied rocks: (1) the very fine grained and unimodal size distribution is similar to those of previously studied pulverized rocks (Muto et al., 2015; Schröckenfuchs et al., 2015; Williams et al., 2021) and dissimilar to those of polymodal and poorly sorted cataclastic rocks and fault gouges (Reches and Dewers, 2005; Cortinovis et al., 2019; Fig. 9); (2) the distribution in discrete pockets (Fig. 2) is very different from the typical occurrence of fault-parallel (often tabular) bands of cataclastic rocks and fault gouges (e.g. Reches and Dewers, 2005; Williams et al., 2021); and (3) the preservation of primary structures, such as bedding, within the pulverized pockets (Figs. 2b, 2c, and 3a) is typical of all pulverized rocks so far studied (e.g. Ostermeijer et al., 2022, and references therein). Indeed, these latter structures, together with the cemented micro-mosaic breccias (Figs. 5d–5f) surrounding the incoherent pulverized rocks, show that the pulverized dolostone was essentially shattered in situ without significant clast rotations, translations, and shear, as documented for many previously studied pulverized rocks (Dor et al., 2006; Ostermeijer et al., 2022). Moreover, pulverized rocks, both from

370 dolostone (Fondriest et al., 2017) and from crystalline rocks (Rempe et al., 2013; Rodríguez-
371 Escudero et al., 2020), are usually characterized by non-systematically oriented fractures
372 separating the single grains. A non-systematic pattern of fractures separating the single
373 grains is also visible in the micro-mosaic breccias studied in this work (Figs. 5e, 5f, and S7-
374 S18).

375

376 ***6.2 Pulverization and Cementation***

377 To understand the pulverization process, we start from some main observations. The
378 first one is that the pulverized dolostone is entirely incohesive and is surrounded by a rock
379 halo, i.e. the proximal host rock, which consists of cemented micro-mosaic breccias, wherein
380 the clasts are still almost in their original position (Figs. 5d–5f) and the related grain size
381 distribution (Figs. 6b) is similar to that of the incohesive pulverized dolostone (Fig.6c).
382 Hence, it seems reasonable to infer that the pulverization process was predominantly dry
383 and was soon followed by rapid calcite cementation in the proximal zones, fossilizing the
384 pulverized pattern and forming a cohesive halo around the incohesive pulverized dolostone.
385 In other words, the incohesive pulverized dolostone and the surrounding cemented micro-
386 mosaic breccias (or proximal host rock) witnessed a primary dry pulverization and secondary
387 cementation through $CaCO_3$ precipitation immediately following the pulverization itself. The
388 banded pattern, in places, of the calcite cement (Figs. 5d, S2d, and S19) indicates
389 successive cycles of crystal (cement) growth, but we cannot determine the rate (rapid vs.
390 slow) of successive band development.

391 The combination of mineralogical and geochemical evidence and micro-structural
392 observations help us to better understand the pulverization and cementation processes. We
393 stress the fact that the host rock is very heterogeneous, with varying amounts of calcite and
394 dolomite constituting the two endmembers (Fig. 7). Therefore, we cannot infer whether the

pulverization process chemically altered one of the endmembers (calcite and dolomite); however, the pulverized pockets are almost entirely made up of dolomite (average content = 98%; Fig. 7). This evidence suggests that the pulverization process was localized within almost pure dolostone, as previously observed elsewhere in faulted carbonates (e.g. Fondriest et al., 2017). Since, in fact, the pulverization process often operates by breaking apart the crystal boundaries (inter- rather than intra-crystalline fractures; Doan and Billi, 2011), the microcrystalline texture of (sedimentary) limestone can prevent the pulverization itself due to an excessive energy necessary to break apart every micro-crystalline boundary. The exception is the Carrara marble, which is macrocrystalline and can be pulverized under certain circumstances (e.g. Doan and Billi, 2011). Also dolostone is often macrocrystalline and thus can be pulverized more easily than microcrystalline sedimentary limestone (Fondriest et al., 2017; Kaminskaite et al., 2020).

In the same way as the mineralogical analyses, also bulk geochemical analyses (i.e., where the calcite cement was not separated by the host rock) do not allow us to identify sharp differences in minor elements or REE between the analyzed rocks (Fig. 8). Yet, the punctual isotope analyses on the calcite cement show a different pattern with respect to the rest of the analyzed samples (Figs. 8a and 8b). In particular, the reduced values of $\delta^{18}O$ (around 27 instead of 30 ‰ V-SMOW) and the increasing values of $\delta^{13}C$ (from 3 to almost 8 ‰ V-PDB) for the calcite cement analyzed in sample A1.1 (Figs. 8a, 8b, and S19) are compatible with a trend of isotope fractionation of carbon dissolved in water due to calcite precipitation (i.e. the cement in our case) from a parent solution that rapidly degassed CO_2 (Baldermann et al., 2020). Di Luccio et al. (2018) found similar carbon isotope values (from 3 to 8 ‰ V-PDB) in active springs in the Matese area and ascribed this pattern to CO_2-degassed waters possibly containing a deep CO_2 contribution.

The above-mentioned structural and geochemical evidence, particularly the fact that the studied pulverized pockets are completely incohesive inside and surrounded by a halo of cemented micro-mosaic breccias, lets us think that the process of pulverization must have been somehow driven mainly by gases and related temporal pressure fluctuations. In fact, if the system would have been dominated by CO_2-rich groundwaters, we would probably also have had calcite pervasive precipitation within the pulverized pockets, particularly in a territory dominated by carbonate successions and active CO_2-degassing and hence by bicarbonate-saturated groundwaters. We might exclude, on the other hand, pulverization processes previously proposed and including compression during supershear ruptures (Doan and Gary, 2009), tensile loading by wrinkle-like ruptures on bi-material faults (Ben-Zion and Shi, 2005), rapidly oscillating stresses during a single rupture (Braunagel and Griffith, 2019), and accumulation through repeated sub-Rayleigh ruptures, either in tension (Griffith et al., 2018) or compression (Aben et al., 2016). These processes, in fact, generate large masses of pulverized rocks rather than the series of meters-sized discrete pockets of pulverization observed in our study area (Fig. 2).

We therefore suggest that the dolostone pulverization studied in this paper was mainly driven by discrete gas accumulations and pressure fluctuations within restricted volumes of rocks prone to be pulverized for their internal structure. This hypothesis is well supported by the large output of deeply-sourced CO_2-rich gases in the study area (Italiano et al., 2000; Caracausi and Paternoster, 2015; Di Luccio et al., 2018; Ascione et al., 2019). Thus, the aforementioned pulverization process by rapid decompression of the gas trapped in the rock (Mitchell et al., 2013; see also Wang et al., 2015 and Pan et al., 2020) becomes a valid candidate to explain the formation of the studied rocks. Such a process would involve a rapid expansion of a trapped gas (i.e., unable to quickly drain out of the rock) within the rock due to a rapid decompression and consequent micro-fragmentation of the host rock (pulverization). However, it cannot be excluded that the decompression pulverization

445 process was enhanced by a previous decrease of rock strength due to chemical corrosion
446 by circulating aggressive fluids.

447 In addition to the occurrence of the discrete meters-sized pockets and the massive
448 venting of CO_2-rich gases, the following facts further support the hypothesis of a
449 pulverization driven by gas pressure changes. The dolomitic host rock has a primary
450 intergranular microporosity (Figs. 5a–5c). This microporosity may have generated the
451 appropriate level of permeability, suitable to host the gas inside but sufficiently low to prevent
452 its rapid escape during rapid decompression events. Mitchell et al. (2013) demonstrated that
453 pulverization through rapid decompression of gas-saturated rocks can occur solely when
454 intermediate permeability values allow sufficient rock saturation by the gas but hinder any
455 rapid escape of the gas itself. Moreover, our micro-observations and grain size distribution
456 analyses demonstrated that the pulverization process occurred mainly because of inter-
457 rather than intra-crystalline fracturing (Figs. 5e and 5f). In other words, intergranular porosity
458 may have been decisive in localizing fractures between single crystals (interfaces between
459 adjacent crystals) or crystal aggregates. It is noteworthy that the mean size of clasts in the
460 pulverized dolostone (Fig. 6c) is about two–four times higher than the mean size of dolomite
461 crystals in the host rock (Fig. 6a). We infer that the energy that suddenly occupied the
462 studied rocks was not sufficient to further break the rocks themselves and tear apart every
463 single crystal from its neighbors or even fragment the single crystals with intra-crystalline
464 fractures. However, the resulting mean size of the pulverized dolostone clasts is compatible
465 with the mean size range of previously studied fault-related pulverized rocks (Fig. 9).
466 Moreover, the frequent occurrence of clay-rich layers at the top of the pulverized pockets
467 (Fig. 3e) suggests that the gas could have accumulated in what are now the pulverized
468 pockets, in part (but not exclusively) due to the sealing effect exerted by the clay-rich layers.
469 The presence, immediately around the pulverized pockets, of pulverized tubercles within the
470 host rock suggests the occurrence of gas saturation and the subsequently pulverized

471 tuberculous apophyses branching off from the main pockets. The $CaCO_3$-cements that
472 fossilized the micro-mosaic breccias around the pulverized pockets is cryptocrystalline and
473 equigranular, and this fossilized a micro-mosaic breccia that is known to develop impulsively
474 (Melosh et al., 2014). Hence, a reasonable hypothesis is that this cement formed impulsively
475 too in connection with the pulverization. An explanation may be that rapidly decompressed
476 and pulverized pockets attracted, due to the difference in pressure, nearby bicarbonate-rich
477 waters from which cryptocrystalline calcite rapidly precipitated in the decompressed and
478 pulverized pockets. The isotope data discussed above (Figs. 8a and 8b) support the
479 precipitation of the calcite cement from a CO_2-degassed groundwater. Such a precipitation
480 would have quickly formed an impermeable halo around the incohesive pockets, which
481 would therefore have remained protected from further mineralizing fluids. It is noteworthy
482 that these sealing halos formed not only at the outcrop-scale but also at the micro-scale
483 (Figs. 5h and 5i). The same type of sealing halo was also found in coseismic micro-scale
484 pulverized and cemented carbonates along the Mt. Morrone fault (see figure S2d in Coppola
485 et al., 2021).

486 The model of pulverization by rapid decompression of gas-saturated rocks proposed
487 by Mitchell et al. (2013) implies a disruptive event necessary to suddenly lower the pore
488 pressure in the rock. We hypothesize that this type of disruptive event may be an earthquake
489 that suddenly modulated the permeability of the saturated rocks (in addition to the coseismic
490 stress drop), hence causing a dramatic and rapid decompression. The study area is indeed
491 a highly seismic one (Boncio et al., 2022), and the relationship between rock pulverization
492 and high-energy earthquakes has been proposed several other times (Ostermeijer et al.,
493 2022, and references therein). Using the words by Rowe and Griffith (2015): “At high strain
494 rates, the transition from discrete fracture to pulverization is governed by the rate sensitivity
495 of fracture toughness, adding evidence that rock pulverization is a true signature of high
496 strain rate deformation that can only be achieved during earthquake rupture or

497 extraterrestrial impacts (Bhat et al., 2012).” We acknowledge, however, that in our study
498 case, a cause–effect relationship between earthquakes and dolostone pulverization is highly
499 speculative and should be further investigated and validated. At present, no more plausible
500 causes than an earthquake can be proposed for the sudden decompression of the studied
501 rock system. To this end, as mentioned above, it is noteworthy that some structures
502 observed around the pulverized pockets were also observed in coseismic microlayers along
503 the Mt. Morrone fault in the central Apennines (compare Figs. 5h and 5i in this work with
504 figure S2d in Coppola et al., 2021). We refer in particular to the pulverized dolostone
505 cemented by microsparry calcite that surrounded and, in some cases, shielded relicts of
506 uncemented pulverized dolostone. However, we cannot exclude, for example, that the rapid
507 decompression was generated by the sudden breaking of a permeability barrier due to the
508 accumulation of pressurized fluids itself or to the energy radiated by a nearby volcanic
509 eruption.

510

511 ***6.3 Model and implications***

512 Fig. 10 synthesizes our view of the studied pulverization process:

513 (1) During interseismic phases, CO_2-rich gases accumulated at the top of a
514 bicarbonate-rich aquifer in meters-sized pockets of dolostone that are
515 characterized by primary intergranular porosity. The gas was provided by deep
516 sources (crust and mantle) at local and regional scale (e.g. Caracausi and
517 Paternoster, 2015; Di Luccio et al., 2018).
518 (2) During disruptive events, likely high-energy seismic events, the gas underwent
519 rapid decompression. Where the permeability was sufficiently low to prevent a
520 prompt escape of the gas from the rock, the sudden expansion of the trapped gas
521 within the rock pores pulverized the rock itself.

(3) Shortly after the pulverization, the decompression as well as and the permeability increase enhanced by the failure of intercrystalline bounds attracted the nearby bicarbonate-saturated waters toward the pulverized pockets, where rapid cementation of the pulverized rock occurred due to microsparry calcite precipitation. The rapid cementation formed an impermeable halo around the pulverized dolostone, which therefore remained substantially incohesive, at least in the most internal portion.

Finally, we have no constraints to adequately infer the depth of pulverization. Tectono-stratigraphic data suggest that the outcrop studied should not have undergone a burial of more than a few kilometers (3.5 km at the minimum). Similar to what was previously suggested for pulverized rocks exposed elsewhere, we believe that pulverization occurred at shallow burial conditions (Yuan et al., 2011). The non-luminescent cement found in the mosaic breccias (Fig. 4h) may indicate a meteoric origin of the cementing fluids, thus limiting the depth of cementation in the shallow crust. Moreover, if our hypothesis of pulverization driven by rapid decompression of CO_2-rich gases is viable, then this process should have occurred above the boundary between the subcritical gaseous CO_2 (above) and the supercritical CO_2 (midway between a gas and a liquid) at approximately 800 m depth (van der Meer et al., 2009). The rapid decompression model implies indeed a rapid expansion that is a property of gases and not liquids. Considering this depth limit (800 m), we can further speculate on the age of the pulverization process by considering the average exhumation rate of 0.5 mm/yr that seems valid for most parts of the Apennines (Erlanger et al., 2022 and references therein). By multiplying this rate with the hypothetical maximum depth of the pulverization process (800 m), we obtain a hypothetical maximum age of 400 ka for the studied pulverized rocks. This age matches the period of main eruptive activities in the nearby Roccamonfina Volcano (main eruptive stages at 439 ± 9, 354 ± 5, 331 ± 2, 230, and 148 ± 9 ka; Rouchon et al., 2008), which, during Pleistocene time, must have been

548 the main source of CO_2 in the studied area, thus strengthening our hypothesis of dolostone
549 pulverization linked with gas venting and rapid decompression in the shallow crust.
550 Therefore, from volcanic (Rouchon et al., 2008) and tectonic data (Boncio et al., 2022), we
551 infer that, during the Pleistocene, in times younger than about 500 ka, the southern margin
552 of the Matese Mts. was an ideal spot where processes of pulverization such as that proposed
553 in this paper may have occurred due to the seismic activity connected with active normal
554 faults and CO_2-rich fluid (gas) circulation connected with active volcanism. Both seismic
555 activity and CO_2-rich fluid circulation are still active in the area.

556

557 ## 7. Conclusions

558 Different lines of evidence from the southwestern margin of the Matese Mts. in Italy
559 allow us to describe a new mechanism for rock (dolostone) pulverization, which has never
560 been documented or proposed for natural active tectonic environments (only for laboratory
561 experiments). This mechanism implies a gas saturation of rock during the interseismic phase
562 (CO_2-rich gases, in our case) and coseismic rapid decompression that makes the gas rapidly
563 expand within the rock, thus pulverizing the host rock in situ. As shown by previous
564 laboratory experiments (Mitchell et al., 2013), this mechanism can only work when there are
565 appropriate intervals of permeability that hinder the rapid escape of the gas from the rock.
566 We believe that this mechanism should be further explored, documented, and validated
567 elsewhere before being considered as a viable process of (coseismic) deformation in active
568 tectonic environments. It is, however, a process to consider when operating subsurface CO_2
569 storage. A rapid decompression of the stored CO_2 may indeed dramatically shatter the host
570 rock and change its physical properties.

571

Acknowledgements

We acknowledge no funding for this study except the ordinary institutional ones (i.e. from authors' institutions).

References

Aben, F.M., Doan, M.-L., Mitchell, T.M., Toussaint, R., Reschla, T., Fondriest, M., Gratier, J.-P., Renard, F., 2016. Dynamic fracturing by successive coseismic loadings leads to pulverization in active fault zones. Journal of Geophysical Research, 121, 2338–23360

Aben, F.M., Doan, M.-L., Gratier, J.-P., Renard, F., 2017. High strain rate deformation of porous sandstone and the asymmetry of earthquake damage in shallow fault zones. Earth and Planetary Science Letters, 463, 81–91.

Agosta, F., Kirschner, D.L., 2003. Fluid conduits in carbonate-hosted seismogenic normal faults of central Italy. Journal of Geophysical Research, 108, 2221, doi:10.1029/2002JB002013.

Agosta, F., Aydin, A., 2006. Architecture and deformation mechanism of a basin bounding normal fault in Mesozoic platform carbonates, Central Italy. Journal of Structural Geology, 28, 1445-1467.

Alidibirov, M., Dingwell, D., 1996. Magma fragmentation by rapid decompression. Nature 380, 146–148.

Ascione, A., Ciotoli, G., Bigi, S., Buscher, J., Mazzoli, S., Ruggiero, L., Sciarra, A., Tartarello, M.C., Valente, E., 2018. Assessing mantle versus crustal sources for non-volcanic degassing along fault zones in the actively extending southern Apennines mountain belt (Italy). Geological Society of America Bulletin,130, 1697–1722.

Baldermann, A., Mittermayr, F., Bernasconi, S.M., Dietzel, M., Grengg, C., Hippler, D., Kluge, T., Leis, A., Lin, K., Wang, X., Zünterl, A., Boch, R., 2020. Fracture dolomite as an archive of continental palaeo-environmental conditions. Communications Earth & Environment, 1, 35, https://doi.org/10.1038/s43247-020-00040-3

Ben-Zion, Y., Shi, Z., 2005. Dynamic rupture on a material interface with spontaneous generation of plastic strain in the bulk. Earth and Planetary Science Letters, 236, 486-496.

Bhat, H.S., Rosakis, A.J., Sammis, C.G., 2012. A micromechanics based constitutive model for brittle failure at high strain rates. Journal of Applied Mechanics, 79, 031016,

Boncio, P., Auciello, E., Amato, V., Aucelli, P., Petrosino, P., Tangari, A.C., Jicha, B., 2022. Late Quaternary faulting in the southern Matese (Italy): implications for earthquake potential and slip rate variability in the southern Apennines. Solid Earth, 13, 553–582.

Braunagel, M.J., Griffith, W.A., 2019. The effect of dynamic stress cycling on the compressive strength of rocks. Geophysical Research Letters, 46, 6479–6486.

Brune, J.N., 2001. Fault normal dynamic loading and unloading: an explanation for ‘‘non-gouge’’ rock powder and lack of fault-parallel shear bands along the San Andreas fault. EOS Trans. Am. Geophys. Union, 82.

Caracausi, A., Paternoster, M., 2015. Radiogenic helium degassing and rock fracturing: A case study of the southern Apennines active tectonic region. Journal of Geophysical Research, 120, 2200-2211, doi:10.1002/2014JB011462.

Castorina, F., Masi, U., Billi, A., 2020. Assessing the origin of Sr and Nd isotopes and (REE+Y) in Middle-Upper Pleistocene travertines from the Acquasanta Terme area

(Marche, central Italy) and implications for neotectonics. Applied Geochemistry, 117, 104596.

Chiodini, G., Caliro, S., Cardellini, C., Granieri, D., Avino, R., Baldini, A., Donnini, M., Minopoli, C., 2010. Long-term variations of the Campi Flegrei, Italy, volcanic system as revealed by the monitoring of hydrothermal activity. Journal of Geophysical Research, 115, B03205, https://doi.org/10.1029/2008JB006258.

Coppola, M., Correale, A., Barberio, M.D., Billi, A., Cavallo, A., Fondriest, M., Nazzari, M., Paonita, A., Romano, C., Stagno, V., Viti, C., Vona, A., 2021. Meso- to nano-scale evidence of fluid-assisted co-seismic slip along the normal Mt. Morrone Fault, Italy: implications for earthquake hydrogeochemical precursors. Earth and Planetary Science Letters, 568, 117010, https://doi.org/10.1016/j.epsl.2021.117010.

Cortinovis, S., Balsamo, F., Storti, F., 2019. Influence of analytical operating procedures on particle size distributions in carbonate cataclastic rocks. Journal of Structural Geology, 128,103884, https://doi.org/10.1016/j.jsg.2019.103884

Di Luccio, F., Chiodini, G., Caliro, S., Cardellini, C., Convertito, V., Pino, N.A., Tolomei, C., Ventura, G., 2018. Seismic signature of active intrusions in mountain chains. Science Advances, 4, e1701825.

Doan, M.-L., Gary, G., 2009. Rock pulverization at high strain rate near the San Andreas fault. Nature Geoscience, 2, 709–712.

Doan, M.-L., Billi, A., 2011. High strain rate damage of Carrara marble. Geophysical Research Letters, 38, L19302, https://doi.org/10.1029/2011GL049169

Dor, O., Ben-Zion, Y., Rockwell, T.K., Brune, J., 2006. Pulverized rocks in the Mojave section of the San Andreas Fault Zone. Earth and Planetary Science Letters, 245, 642–654.

Erlanger, E.D., Fellin, M.G., Willett, S.D., 2022. Exhumation and erosion of the Northern Apennines, Italy: new insights from low-temperature thermochronometers. Solid Earth, 13, 347–365, https://doi.org/10.5194/se-13-347-2022

Fondriest, M., Doan, M.L., Aben, F., Fusseis, F., Mitchell, T.M., Voorn, M., Secco, M., Di Toro, G., 2017. Static versus dynamic fracturing in shallow carbonate fault zones. Earth and Planetary Science Letters, 461, 8–19.

Griffith, W.A., St. Julien, R.C., Ghaffari, H.O., Barber, T.J., 2018. A tensile origin for fault rock pulverization. Journal of Geophysical Research,123, 7055–7073.

Italiano, F., Martelli, M., Martinelli, G., & Nuccio, P. M. (2000). Geochemical evidence of melt intrusions along lithospheric faults of the Southern Apennines, Italy: geodynamic and seismogenic implications. Journal of Geophysical Research: Solid Earth, 105(B6), 13569-13578.

Kaminskaite, I., Fisher, Q.J., Michie, E.A.H., 2020. Faults in tight limestones and dolostones in San Vito lo Capo, Sicily, Italy: internal architecture and petrophysical properties. Journal of Structural Geology, 132, 103970.

Malinverno, A., Ryan, W.B., 1986. Extension in the Tyrrhenian Sea and shortening in the Apennines as result of arc migration driven by sinking of the lithosphere. Tectonics, 5, 227-245.

Melosh, B.L., Rowe, C.D., Smit, L., Groenewald, C., Lambert, C.W., Macey, P., 2014. Snap, Crackle, Pop: Dilational fault breccias record seismic slip below the brittle–plastic transition. Earth and Planetary Science Letters, 403, 432-445.

Mitchell, T.M., Ben-Zion, Y., Shimamoto, T., 2011. Pulverized fault rocks and damage asymmetry along the Arima Takatsuki Tectonic Line, Japan. Earth and Planetary Science Letters, 308, 284–297.

Mitchell, T.M., Billi, A., Miller, S.A., Goldsby, D.L., Scholz, C.H., Gran, J. K., Simons, J., 2013. Dynamic pulverization by rapid decompression. Eos Transactions AGU, Fall Meeting Supplement, Abstract MR41B–04.

Mostardini, F., Merlini, S., 1986. Appennino centro merdionale. Sezioni geologiche e proposta di modello strutturale. Memorie della Società Geologica Italiana, 35, 177-202.

Muto, J., Nakatani, T., Nishikawa, O., Nagahama, H., 2015. Fractal particle size distribution of pulverized fault rocks as a function of distance from the fault core. Geophysical Research Letters, 42, 3811–3819, https://doi.org/10.1002/2015GL064026

O'Nions, R.K., Oxburgh, E.R., 1988. Helium, volatile fluxes and the development of continental crust. Earth and Planetary Science Letters, 90, 331-347, doi:10.1016/0012-821x(88)90134-3.

Ostermeijer, G.A., Aben, F.M., Mitchell, T.M., Rockwell, T.K., Rempe, M., Farrington, K., 2022. Evolution of co-seismic off-fault damage towards pulverization. Earth and Planetary Science Letters, 579, 117353.

Pan, X., Cheng, H., Chen, J., Zhou, X., 2020. An experimental study of the mechanism of coal and gas outbursts in the tectonic regions. Engineering Geology, 279, 105883, https://doi.org/10.1016/j.enggeo.2020.105883

Randazzo, P., Caracausi, A., Aiuppa, A., Cardellini, C., Chiodini, G., D'Alessandro, W., Li Vigni, L., Papic, P., Marinkovic, G., Ionescu, A., 2021. Active degassing of deeply sourced fluids in central Europe: new evidences from a geochemical study in Serbia. Geochemistry, Geophysics, Geosystems, 22, e2021GC010017, https://doi.org/10.1029/2021GC010017

Reches, Z., Dewers, T.A., 2005. Gouge formation by dynamic pulverization during earthquake rupture. Earth and Planetary Science Letters, 235, 361-374.

Rempe, M., Mitchell, T., Renner, J., Nippress, S., Ben-Zion, Y., Rockwell, T., 2013. Damage and seismic velocity structure of pulverized rocks near the San Andreas Fault, Journal of Geophysical Research, 118, 2813–2831.

Rockwell, T., Sisk, M., Girty, G., Dor, O., Wechsler, N., Ben-Zion, Y., 2009. Chemical and physical characteristics of pulverized Tejon Lookout granite adjacent to the San Andreas and Garlock Faults: implications for earthquake physics. Pure and Applied Geophysics, 166, 1725–1746.

Rodríguez-Escudero, E., Martínez-Díaz, J.J., Giner-Robles, J.L., Tsige, M., Cuevas-Rodríguez, J., 2020. Pulverized quartz clasts in gouge of the Alhama de Murcia fault (Spain): Evidence for coseismic clast pulverization in a matrix deformed by frictional sliding. Geology, 48, 283–287.

Rouchon, V., Gillot, P.Y., Quidelleur, X., Chiesa, S., Floris, B., 2008. Temporal evolution of the Roccamonfina volcanic complex (Pleistocene), Central Italy. Journal of Volcanology and Geothermal Research,177, 500-514.

Rowe, C.D., Griffith, W.A., 2015. Do faults preserve a record of seismic slip: A second opinion. Journal of Structural Geology, 78, Pages 1-26

Santo, A., Santangelo, N., Balassone, G., Strauss, H., 2019. Deep seated fault-related volcanogenic H_2S as the key agent of high sinkhole concentration areas. Earth Surface Processes and Landforms, 44, 713–735.

Sagy, A., Korngreen, D., 2012. Dynamic branched fractures in pulverized rocks from a deep borehole. Geology, 40, 799–802.

Schröckenfuchs, T., Bauer, H., Grasemann, B., Decker, K., 2015. Rock pulverization and localization of a strike-slip fault zone in dolomite rocks (Salzach–Ennstal–Mariazell–Puchberg fault, Austria). Journal of Structural Geology, 78, 67–85.

van der Meer, L.G.H., Hofstee, C., Orlic, B., 2009. The fluid flow consequences of CO_2 migration from 1000 to 600 metres upon passing the critical conditions of CO_2. Energy Procedia, 1, 3213–3220.

Yuan, F., Prakash, V., Tullis, T., 2011. Origin of pulverized rocks during earthquake fault rupture. Journal of Geophysical Research, 116, B06309, doi: 10.1029/2010JB007721.

Wang, S., Elsworth, D., Liu, J., 2015. Rapid decompression and desorption induced energetic failure in coal. Journal of Rock Mechanics and Geotechnical Engineering, 7, 345-350.

Williams, R.T., Rowe, C.D., Okamoto, K., Savage, H.M., Eves, E., 2021. How fault rocks form and evolve in the shallow San Andreas fault. Geochemistry, Geophysics, Geosystems, 22, e2021GC010092, https://doi.org/10.1029/2021GC010092

Wilson, B., Dewers, T., Reches, Z., Brune, J., 2005. Particle size and energetics of gouge from earthquake rupture zones. Nature, 434, 749–752.

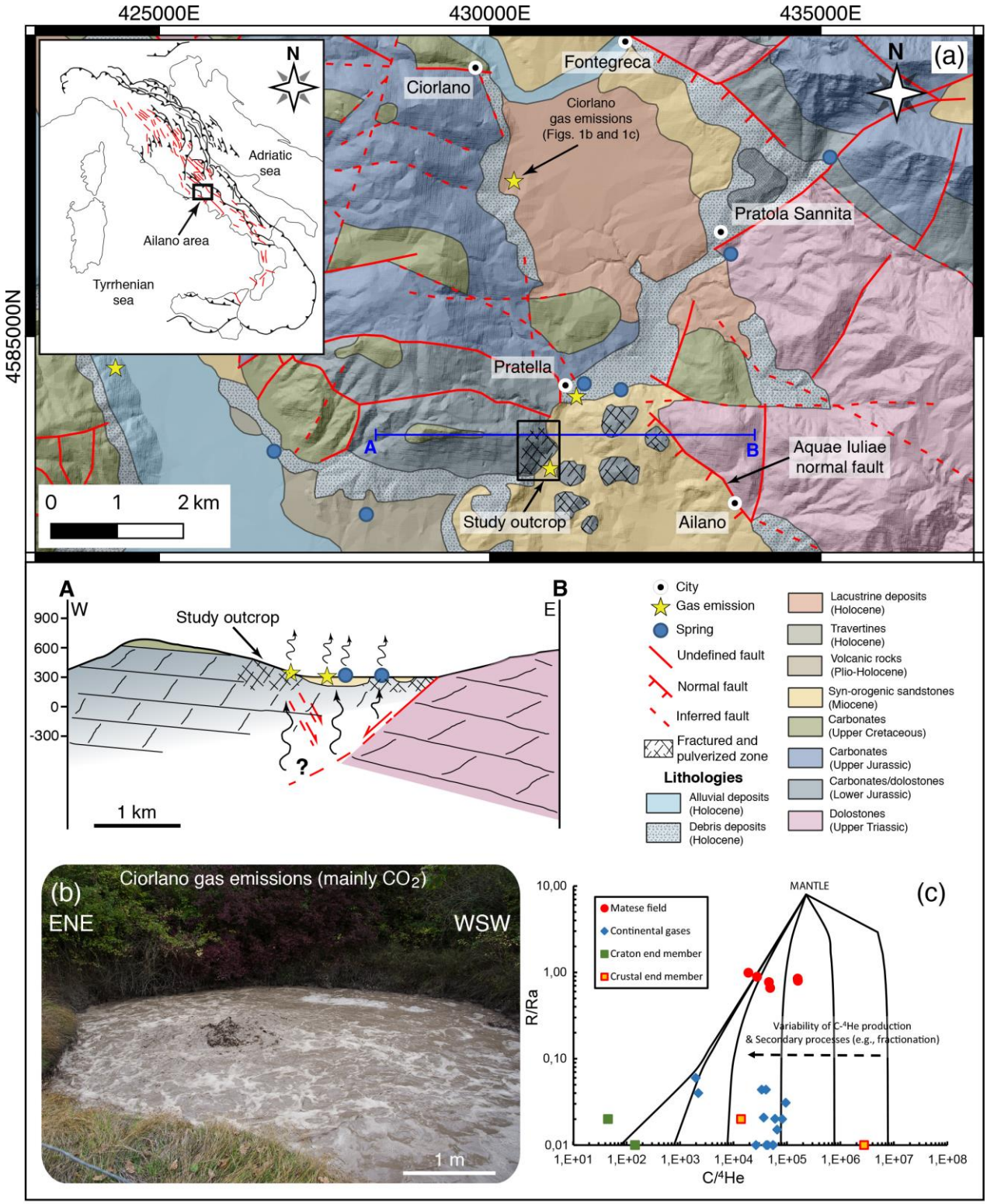

731

732 **Figure 1.** Geological setting. **(a)** Geological setting of the study area. Inset shows location
733 of the study area in Italy, wherein red faults are main active normal faults and black faults
734 are main thrusts. See, below the map, a geological cross-section through the study area,
735 showing that the studied exposure is located at the hanging wall of a normal fault system

with active CO_2-rich springs and vents. **(b)** Photograph of the Ciorlano active CO_2-rich spring nearby the studied rock exposure (see the map for its location). **(c)** Geochemical data from the Ciorlano spring and nearby springs (see the Hydrothermal Setting section for further information). Data plotted in this diagram are in Table S1.

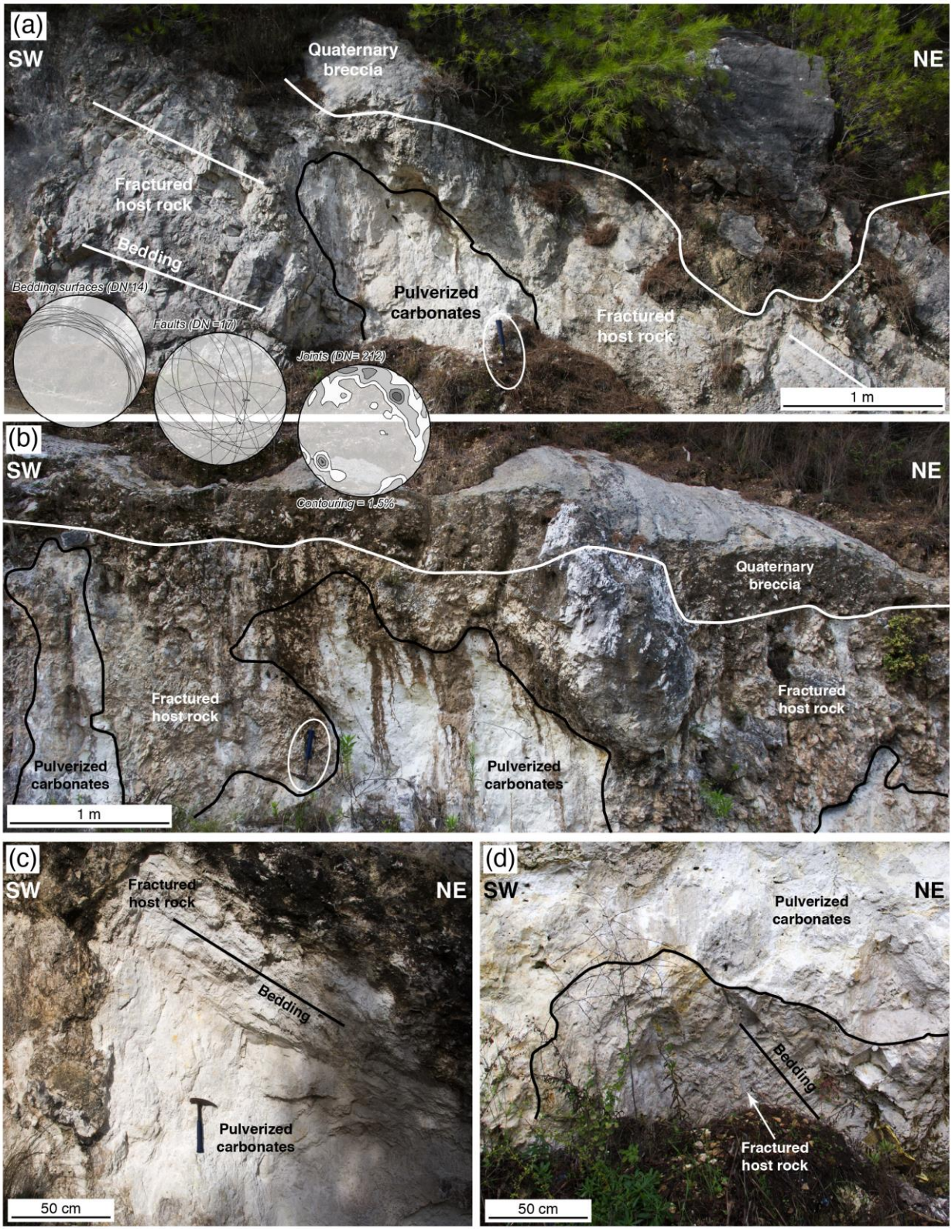

741

742 **Figure 2.** Exposure scale photographs (see also Videos S1-S4 and Virtual Outcrops S1-
743 S4). **(a, b)** Panoramic views of the pulverized dolostones showing domal and chimney-like
744 structures (pulverized pockets in the text) within bedded dolostone. Note the unconformity
745 between the carbonates and the overlying Quaternary slope debris deposits. Three Schmidt

746 polar plots (lower hemisphere; Table S3) in (a) show, from left to right, attitudes of bedding
747 surfaces, normal faults, and joints (represented as contours to joint poles), respectively,
748 measured along the studied exposure. **(c, d)** Pockets of pulverized dolostones where
749 primary structures such as bedding are still preserved although finely pulverized.

750

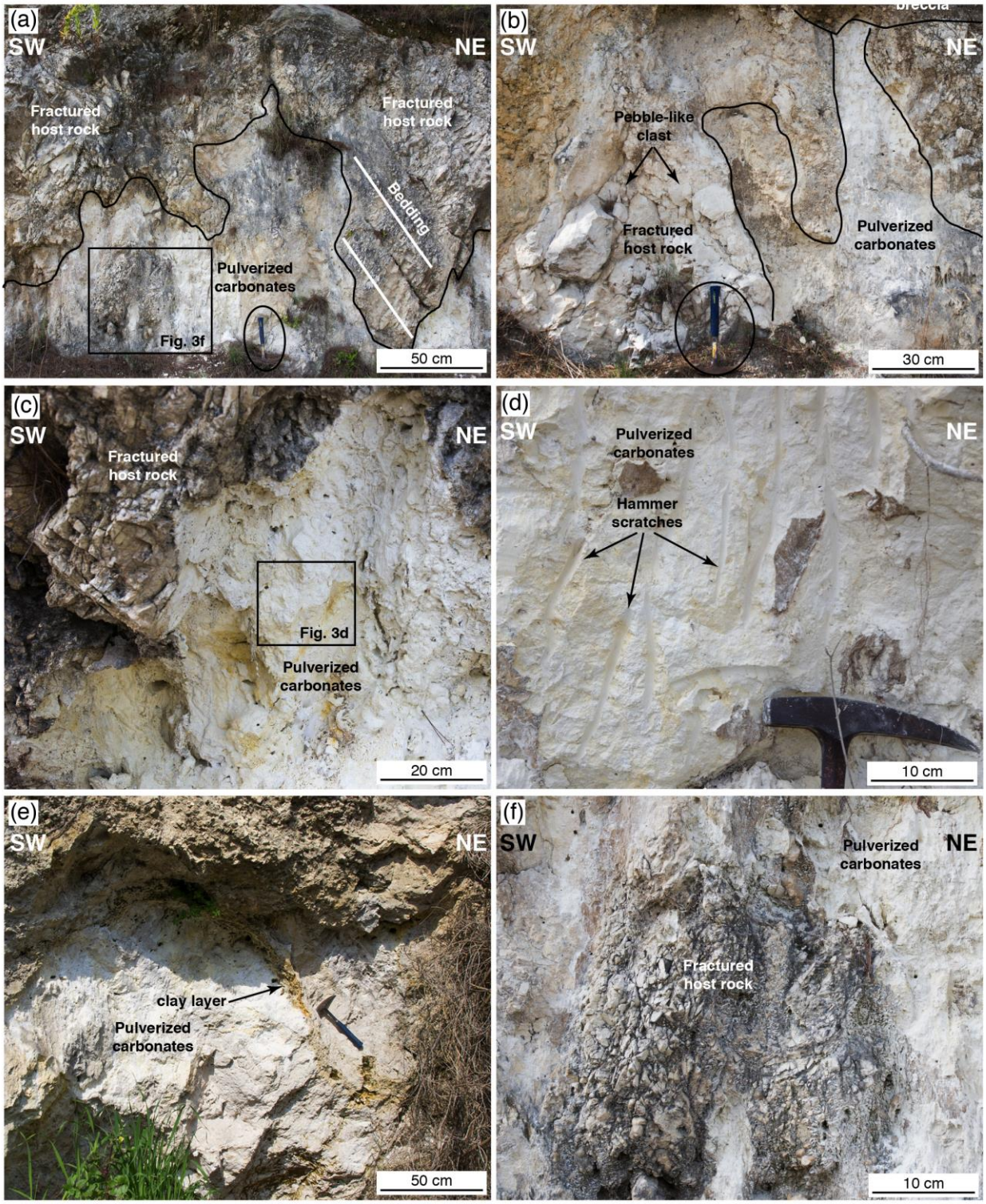

751

752 **Figure 3.** Exposure scale photographs (see also Videos S1-S4 and Virtual Outcrops S1-
753 S4). **(a)** Pockets of pulverized dolostones embedded within highly fractured dolostone beds.
754 **(b)** Pulverized dolostones with preserved pebble-like clasts of host rock. **(c)** Boundary
755 between the pulverized dolostones and the fractured host rock. **(d)** Detail of pulverized

dolostones showing scratches created by the hammer to test the physical status of the rock. **(e)** Antiformal clay-rich layer at the top of a pocket of pulverized dolostones. **(f)** Lens of highly fractured host rock preserved within pulverized dolostones.

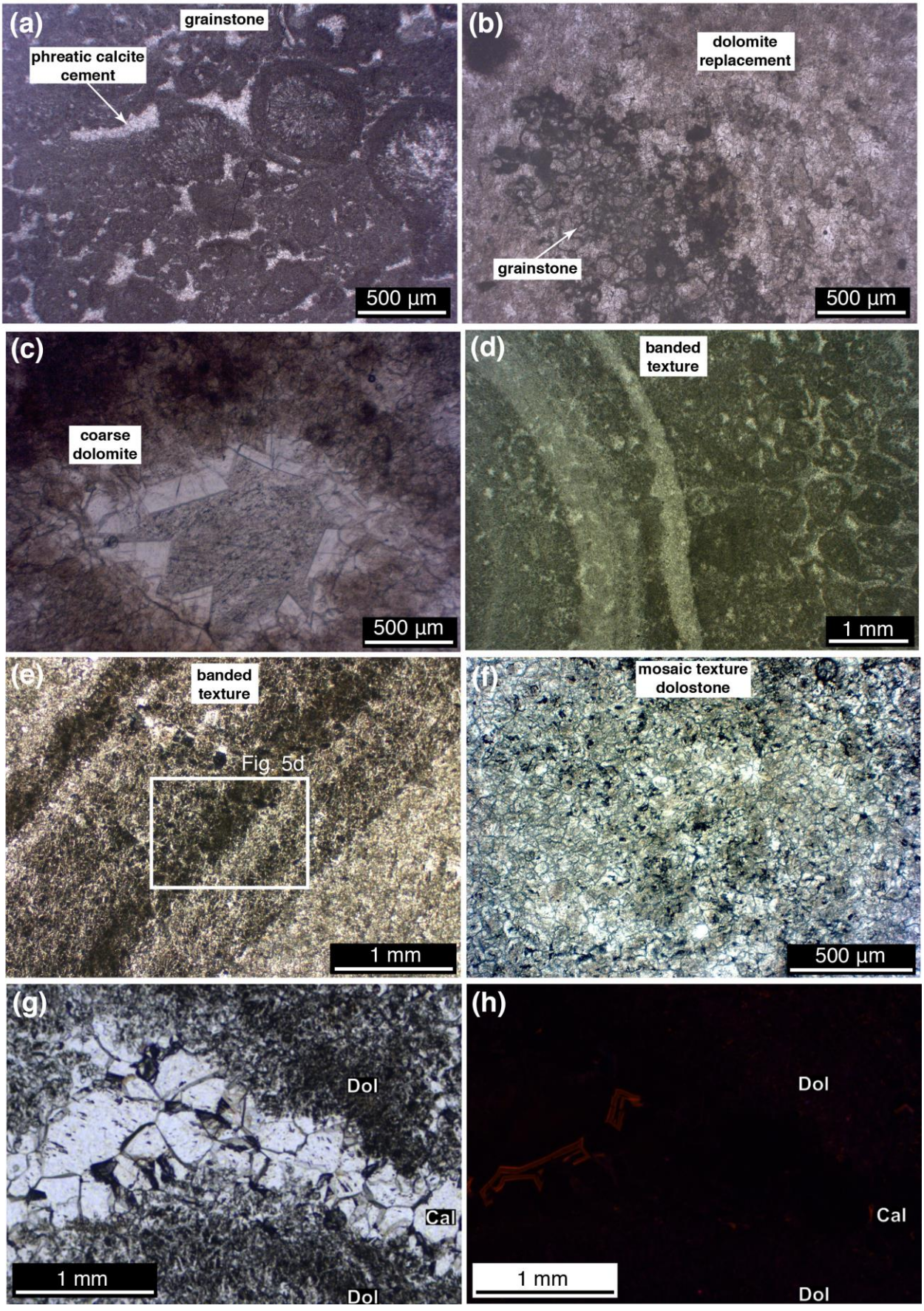
(a)
grainstone
phreatic calcite cement
500 µm
(b)
dolomite replacement
grainstone
500 µm
(c)
coarse dolomite
500 µm
(d)
banded texture
1 mm
(e)
banded texture
Fig. 5d
1 mm
(f)
mosaic texture dolostone
500 µm
(g)
Dol
Cal
1 mm
Dol
(h)
Dol
Cal
1 mm
Dol

760

Figure 4. Microscopic photographs (see also Figs. S1-S4). **(a,b)** Distal carbonate host rock showing primary depositional features and evidence of diagenetic dolomitization. **(c)** Coarse secondary dolomite filling a void within distal carbonate host rock. **(d)** Proximal fractured host rock collected close to the pulverized dolostones, showing a banded texture. **(e)** Detail of banded texture showing fine-grained dolomite crystals. **(f)** Mosaic or crackle-like texture within the fine-grained dolomite crystals. **(g,h)** Calcite crystals filling a fracture and showing a dull red zoned luminescence color.

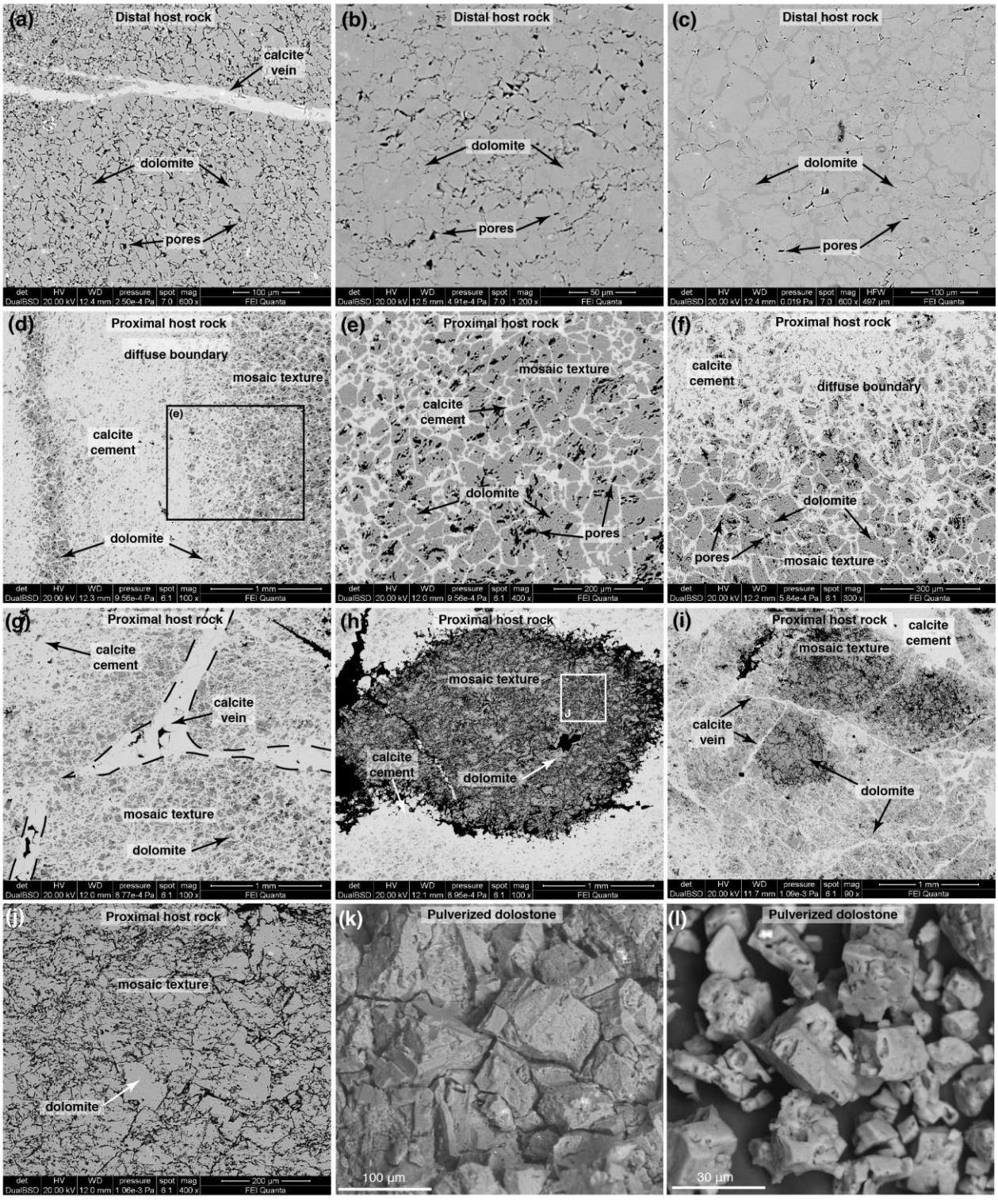

769

770 **Figure 5.** Microscopic photographs (see also Figs. S1-S4). **(a-c)** Microscale texture of the
771 distal carbonate host rock showing fine-grained dolomite crystals cut, in (a), by a calcite filled
772 vein. **(d)** Proximal host rock showing a banded texture with alternating bands made of fine
773 dolomite grains cemented by microcrystalline calcite. **(e,f)** Details of the fine dolomite grains

774 showing a mosaic or crackle-like texture with sharp grain boundaries (e) and a diffuse
775 boundary between the dolomite grains and the microcrystalline calcite (f). **(g)** Calcite filled
776 vein cutting the banded texture. **(h,i)** Proximal host rock showing lenses of fine dolomite
777 grains with a crackle-like texture, sharp grain boundaries, and lack of microcrystalline calcite
778 between the crystals. Compare these microphotographs with figure S2d in Coppola et al.,
779 (2021). **(j)** Detail of fine dolomite grains showing a crackle-like (or masaic) texture and lack
780 of microcrystalline calcite between the grains. **(k,l)** Details of the pulverized and incohesive
781 dolostones characterized by fine dolomite grains with rhomboidal shapes and sharp
782 boundaries.

783

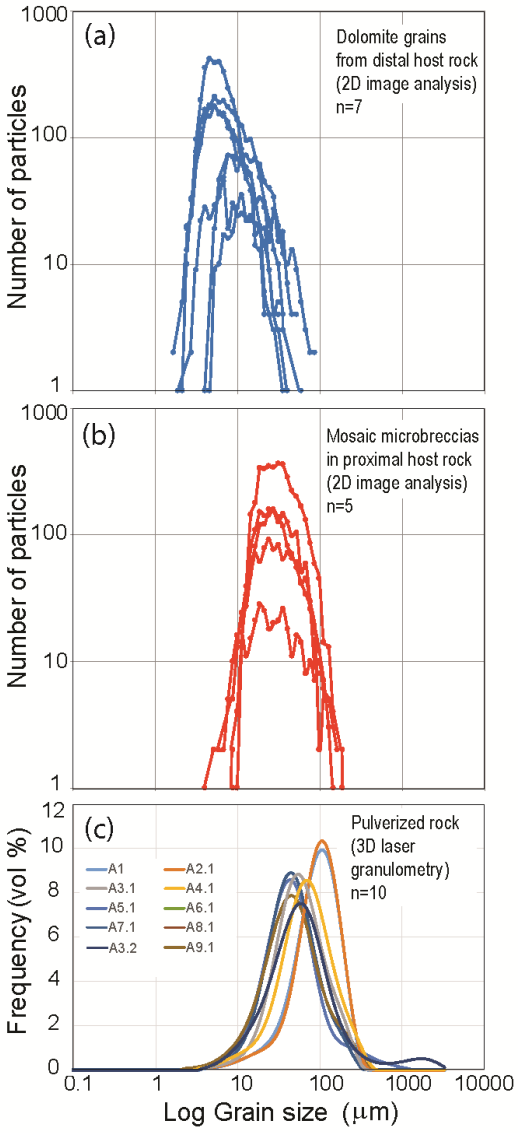
(a)
Dolomite grains
from distal host rock
(2D image analysis)
n=7
Number of particles
1000
100
10
1
(b)
Mosaic microbreccias
in proximal host rock
(2D image analysis)
n=5
Number of particles
1000
100
10
1
(c)
Pulverized rock
(3D laser
granulometry)
n=10
A1
A2.1
A3.1
A4.1
A5.1
A6.1
A7.1
A8.1
A3.2
A9.1
Frequency (vol %)
12
10
8
6
4
2
0
0.1
1
10
100
1000
10000
Log Grain size (µm)

785 **Figure 6.** Grain size distributions (see also Figs. S5-S18 and Tables S4-S5). **(a)** Dolomite
786 grains (i.e. crystals) from distal host rock (2D analysis). **(b)** Dolostone grains (mostly crystal
787 aggregates, more rarely single crystals) from cemented crackle breccias in the proximal host
788 rock (2D analysis). **(c)** Dolostone grains (mostly crystal aggregates, more rarely single
789 crystals) from incohesive pulverized pockets of rocks (3D analysis).

790

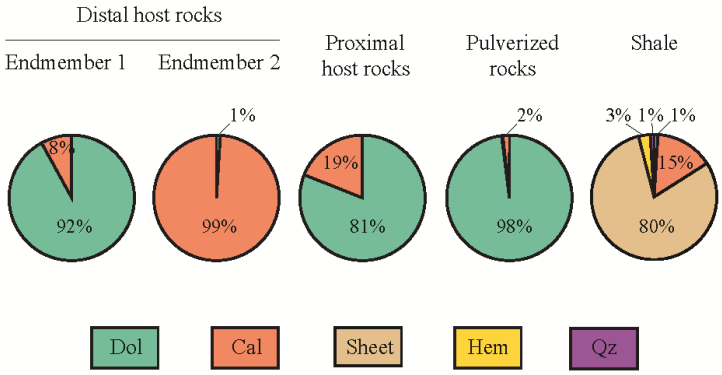
Distal host rocks
Endmember 1
Endmember 2
Proximal host rocks
Pulverized rocks
Shale
8%
92%
1%
99%
19%
81%
2%
98%
3%
1%
1%
15%
80%
Dol
Cal
Sheet
Hem
Qz

Figure 7. X-ray semiquantitative analysis of distal (e.g. Figs. 4a-4c) and proximal (e.g. Figs. 5d-5i) carbonate host rocks, pulverized rocks (e.g. Figs. 5k and 5l), and shales (or clay-rich layers; e.g. Fig. 3e) interbedded with dolostone layers (Table S6). Dol-dolomite, Cal-calcite, Sheet-Sheet silicate, Hem-hematite, Qz-quartz. Numbers refer to average values.

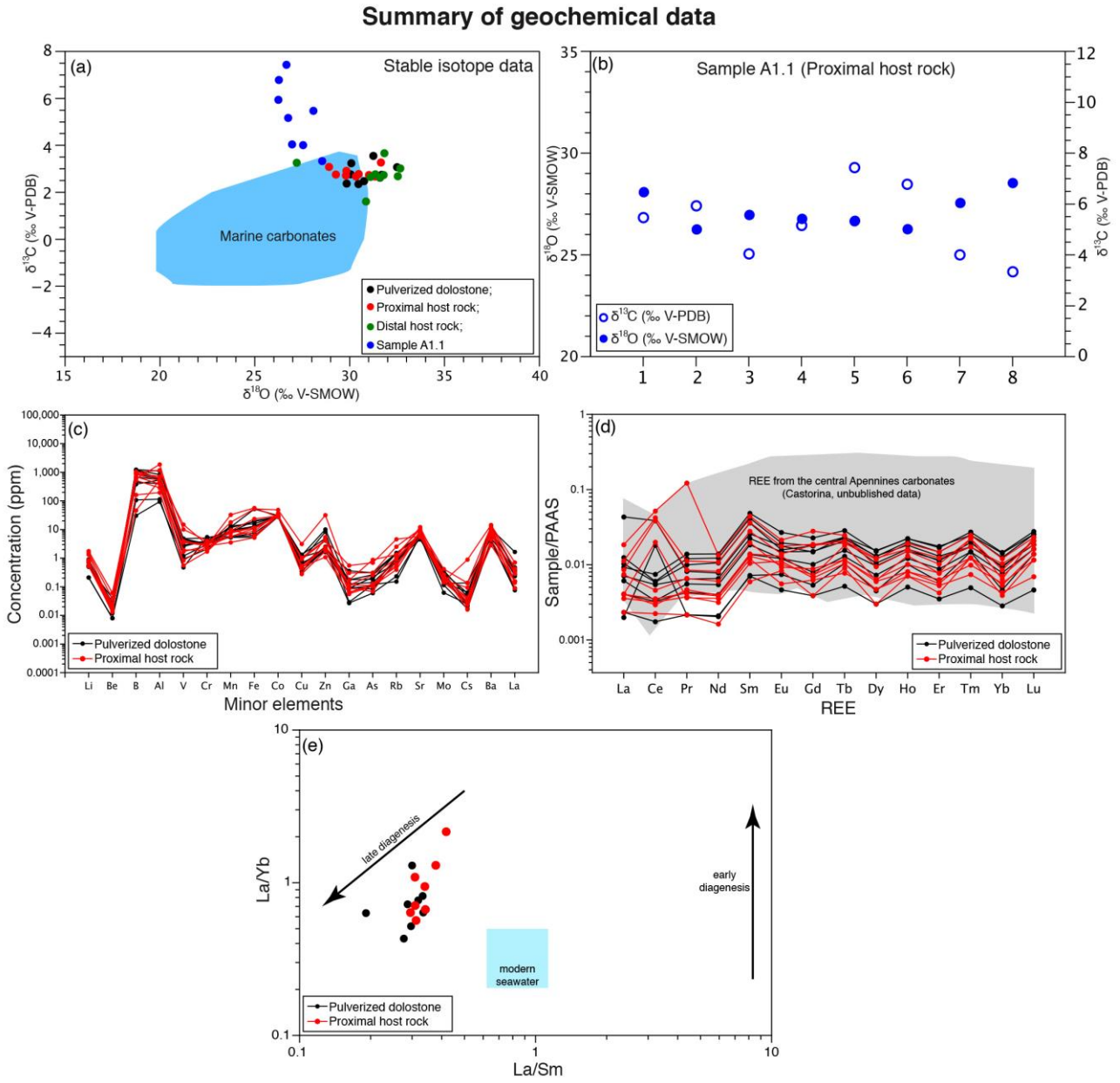

Figure 8. Geochemical data (Tables S7 and S8). **(a)** Diagram showing $\delta^{13}C$ vs. $\delta^{18}O$ values. Note that pulverized carbonates have the same $\delta^{13}C$ and $\delta^{18}O$ values of those from distal

and proximal host rocks (bulk analyses). Micro-subsamples (punctual analysis) of calcite precipitates from sample A1.1 (Fig. S19; proximal host rock) show a large variability of $\delta^{13}C$ values and $\delta^{18}O$ values lower than those of all other samples. **(b)** Diagram showing $\delta^{13}C$ and $\delta^{18}O$ values vs. the sampling distance along the microscale transect (sample A1.1; Fig. S19). **(d)** Diagram for the concentration of minor elements. **(e)** REE concentration vs. Sample/PAAS showing that all the analyzed samples (pulverized carbonates and host rocks) are in the range of REE value or marine carbonates of the central Apennines (bulk chemical analysis). **(f)** La/Sm vs. La/Yb diagram showing that all samples have a late diagenetic imprint (bulk chemical analysis).

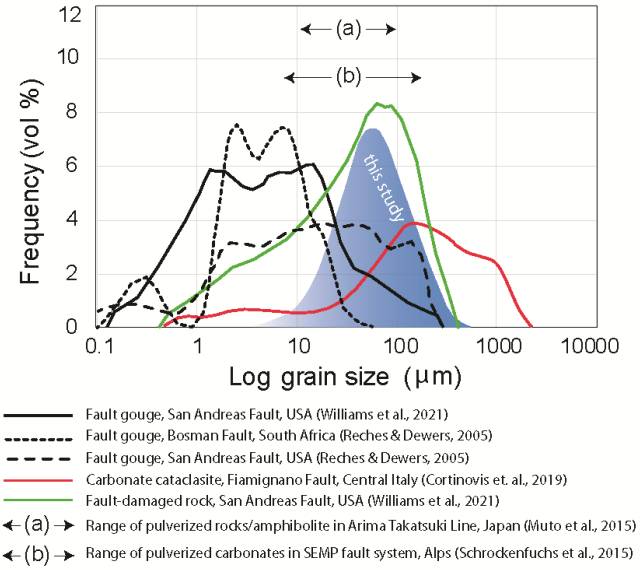
12
10
8
6
4
2
0
Frequency (vol %)
(a)
(b)
this study
0.1
1
10
100
1000
10000
Log grain size (μm)
Fault gouge, San Andreas Fault, USA (Williams et al., 2021)
Fault gouge, Bosman Fault, South Africa (Reches & Dewers, 2005)
Fault gouge, San Andreas Fault, USA (Reches & Dewers, 2005)
Carbonate cataclasite, Fiamignano Fault, Central Italy (Cortinovis et. al., 2019)
Fault-damaged rock, San Andreas Fault, USA (Williams et al., 2021)
(a) Range of pulverized rocks/amphibolite in Arima Takatsuki Line, Japan (Muto et al., 2015)
(b) Range of pulverized carbonates in SEMP fault system, Alps (Schrockenfuchs et al., 2015)

Figure 9. Comparison of grain size distributions between the pulverized rocks studied in this work (average curve in blue) and other fault-related pulverized rocks from the San Andreas Fault in California (Reches and Dewers, 2005; Williams et al., 2021), the Salzach-Ennstal-Mariazell-Puchberg (SEMP) fault system in the Northern Calcareous Alps, Austria (Schrockenfuchs et al., 2015), the Bosman Fault in South Africa (Reches and Dewers, 2005), and the Arima Takatsuki Line in Japan (Muto et al., 2015). For comparison, the grain size distribution curves of carbonate cataclasites and gouges from tectonically active localities in Italy (Cortinovis et al., 2021) are also plotted. Compared to fault-related cataclasites and gouges, the pulverized rocks have narrower grain size ranges and symmetrical, unimodal distributions.

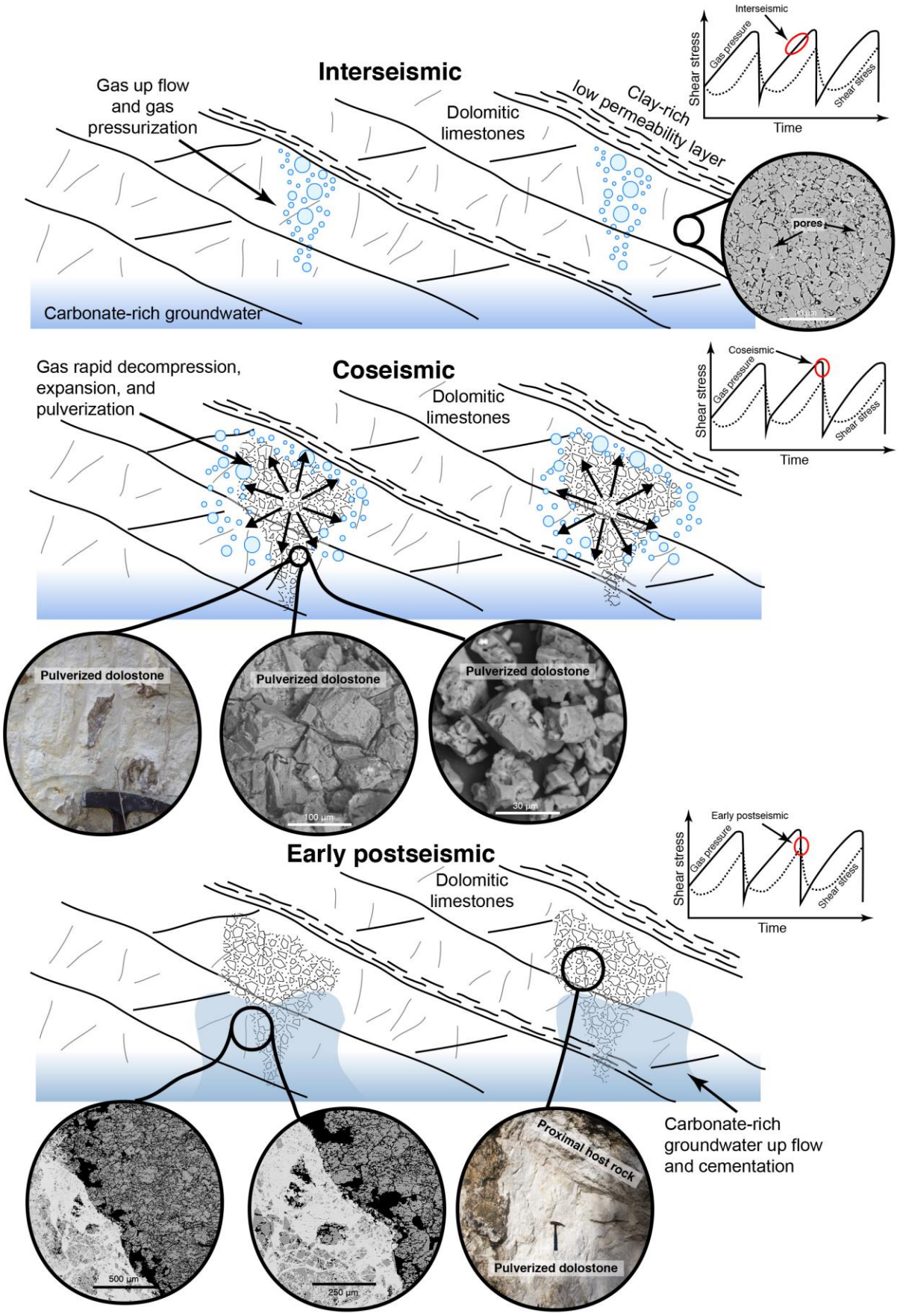
Interseismic
Gas up flow and gas pressurization
Dolomitic limestones
Clay-rich low permeability layer
Carbonate-rich groundwater
pores
Interseismic
Gas pressure
Shear stress
Shear stress
Time
Coseismic
Gas rapid decompression, expansion, and pulverization
Dolomitic limestones
Pulverized dolostone
Pulverized dolostone
Pulverized dolostone
100 µm
30 µm
Coseismic
Gas pressure
Shear stress
Shear stress
Time
Early postseismic
Dolomitic limestones
Carbonate-rich groundwater up flow and cementation
500 µm
250 µm
Proximal host rock
Pulverized dolostone
Early postseismic
Gas pressure
Shear stress
Shear stress
Time

822

Figure 10. Synthetic model of dolostone pulverization. During inter- to pre-seismic stages, CO_2-rich gases accumulate and become pressurized in pockets of microporous dolostones at the top of a bicarbonate-rich aquifer. Likely during coseismic stages, the rock volume is rapidly decompressed and, where the permeability is sufficiently low to prevent a rapid escape of the gas from the rock, the trapped gas itself rapidly expand within the dolomitic rock, pulverizing it in situ. Soon after this stage, the decompression as well as the new porosity generated by the pulverization attracts the bicarbonate-rich waters, which rapidly degas (CO_2) and precipitate a microcrystalline calcite cement that fossilizes the newly pulverized rock forming a cemented micro-mosaic or micro-crackle breccia. The cementation is so rapid that forms a sort of impermeable halo around the pocket of incoherent pulverized dolostone, preventing its cementation.

Table S1

Table S2

Table S3

Table S4

Table S5

Table S6

Table S7

Table S8

Supplemental Diffractograms

Declaration of Interest Statement

The authors declare that they have no known competing financial interests or personal relationships that could have appeared to influence the work reported in this paper.

Credit Author Statement

Andrea Billi: conceptualization, investigation, writing – original draft, supervision, project administration;

Luca Smeraglia: conceptualization ,methodology, validation, formal analysis, investigation, data curation, writing – review & editing;

Luca Aldega: conceptualization, methodology, writing – review & editing, data curation, investigation;

Fabrizio Balsamo: conceptualization, investigation, methodology, writing – review & editing, data curation;

Marino Domenico Barberio: methodology, formal analysis, data curation, review & editing;

Chiara Boschi: conceptualization, investigation, data curation, writing – review & editing;

Antonio Caracausi: conceptualization, investigation, data curation, writing – review & editing;

Eugenio Carminati: conceptualization, investigation, writing – review & editing, supervision, project administration;

Alessandro Iannace: conceptualization, investigation, writing – review & editing, supervision;

Marco Mercuri: validation, formal analysis, investigation, data curation, writing – review & editing, visualization;

Mattia Pizzati: methodology, validation, formal analysis, data curation, , writing – review & editing;

Stefano Tavani: conceptualization, investigation, validation, writing – review & editing, supervision, project administration.